Post-Synthetic Defect Formation in Three-Dimensional Hofmann-Type Coordination Polymers and Its Impact on Catalytic Activity

Daiki Umeyama,*,† Atsuro Takai,† Kazutaka Sonobe§

†Research Center for Functional Materials and §International Center for Materials Nanoarchitectonics, National Institute for Materials Science, 1-1 Namiki, Tsukuba 305-0044, Japan.

ABSTRACT: We report a systematic investigation of post-synthetic defect formation in Hofmann-type coordination polymers $M(pz)[M'(CN)_4]$ ($M = Fe^{2+}$, Co^{2+}, Ni^{2+}; $M' = Pd^{2+}$, Pt^{2+}; pz = pyrazine). These compounds readily undergo selective ligand exchange at the pyrazine site when immersed in methanol (MeOH) at ambient temperature. The ligand exchange changes the chemical formula to $M(pz)_{1-x}(MeOH)_{2x}[M'(CN)_4]$ ($0 < x < 0.3$), affording defective coordination environment around the M ions. The defect concentration is highly dependent on the combination of the metal ions and solvent species, reaching the defect concentration of ca. 30% ($x \sim 0.3$) at maximum. The magnetic state of one such coordination polymer gives an additional control of the defect formation, making the compound less susceptible to the ligand exchange at the low-spin state. Structures that form the defects at high concentration function as catalysts and promote an acetalization reaction heterogeneously by providing Lewis acidic sites. The solvent-dependent character of the defect formation can be used to control the catalytic activity of the active compounds, demonstrating a facile defect engineering for functionalizing solid materials.

1. Introduction

Means of controlling defects are of great importance in materials design, as they strongly influence the properties of materials. In solid-state coordination materials such as coordination polymers (CPs) and metal-organic frameworks (MOFs), defects can be engineered post-synthetically owing to the labile and dynamic character of the coordination bonds.[1-5] Defects in CPs and MOFs are commonly engineered at ligands (linkers), and post-synthetic ligand exchange is used as a tool to enhance the properties of CPs/MOFs such as catalysis and gas adsorption. The method for post-synthetic defect engineering at ligands is also called solvent-assisted linker exchange,[6] being an important technique to obtain structures and properties that are otherwise unattainable. There have been many structures prepared exclusively by defect engineering and solvent-assisted linker exchange.[7-14] However, systematic investigation of defect formation in a single structure with different metal ions has not been sufficiently accumulated.

In this article, we have investigated post-synthetic defect formations in a series of three-dimensional (3D) Hofmann-type CPs, $M(pz)[M'(CN)_4]$ ($M = Fe^{2+}$, Co^{2+}, Ni^{2+}; $M' = Pd^{2+}$, Pt^{2+}; pz = pyrazine; hereafter abbreviated as **MM'**). The structures are characterized by two-dimensional (2D) metal cyanide sheets constructed by the alternate linkage between octahedral M and square-planar M' ions, which is pillared by pyrazine molecules at M ions to form the 3D structure (Figure 1A).[15] These Hofmann-type CPs has been mainly studied for their unique magnetic behaviors such as spin crossover.[16-19] We first focus on its capacity to adapt various metal ions in the isostructure and show that the combinations of the M and M' ions highly influence the concentration of the defects that form post-synthetically. We will also show that the defect formation is strongly coupled with the spin state of the M ion; thus, we can control the defect concentration by the spin state, without changing the chemical composition of the framework. Finally, we demonstrated catalytic acetalization using the defective CPs. Our mechanistic study revealed that the defect concentration was responsible to the catalytic activity. Solvent-dependent nature of the defect formation gave an additional control to the catalytic activity of these CPs.

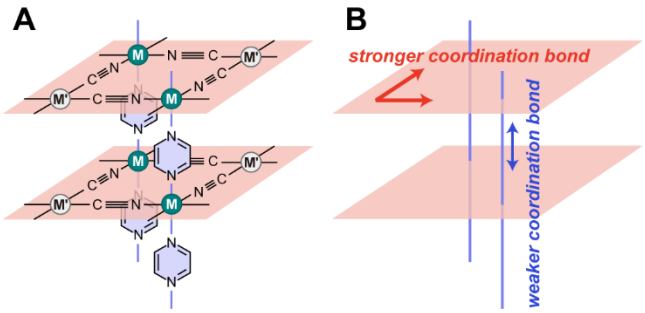

Figure 1. (A) Structure of $M(pz)[M'(CN)_4]$ (**MM'**). (B) Schematic illustration of the stronger and weaker coordination bonds in **MM'**.

2. Experimental Section

2.1. Materials and Methods. All manipulations were conducted in air unless otherwise noted. The mesostructured aluminosilicate (MCM-41 type) was purchased from Sigma-Aldrich (Product Number 643653) and heated at 393 K under reduced pressure prior to use. Other reagents were purchased from commercial vendors and used as received. The solvents methanol (MeOH), ethanol (EtOH), isopropyl alcohol (IPA), acetone, tetrahydrofuran (THF), acetonitrile (MeCN), and dichloromethane (DCM) were anhydrous and deoxidized grade. Powder crystals of $M(pz)[M'(CN)_4]$ were prepared according to modified literature procedures.[15] Details of sample synthesis are given in the Supporting Information.

2.2. Powder X-ray diffraction (PXRD). Room-temperature PXRD measurements were performed under ambient conditions on a Rigaku MiniFlex600 diffractometer equipped with a Cu anode

($K\alpha_1$ = 1.54060 Å, $K\alpha_2$ = 1.54443 Å, $K\alpha_2/K\alpha_1$ = 0.5), fixed divergence slits with a nickel filter, and a D/teX Ultra detector. Variable-temperature PXRD measurements were performed on Rigaku SmartLab diffractometer equipped with a Cu anode ($K\alpha_1$ = 1.54060 Å, $K\alpha_2$ = 1.54443 Å, $K\alpha_2/K\alpha_1$ = 0.5), an automatic variable divergence slit, a HyPix 3000 detector, and a TTK600 low temperature chamber. These instruments were operated in a Bragg-Brentano geometry with a step size of 0.02 ° (2θ).

2.3. Optical measurements. The powders of M(pz)[M'(CN)$_4$] (80.0 μmol) was suspended in 4 mL dry MeOH for 30 minutes. The suspension was filtered to obtain colorless, transparent filtrates. The filtrates were diluted by 20 times with MeOH. UV-Vis absorption measurements were taken using a Shimadzu UV-2450 spectrometer in transmission mode.

2.4. Gas chromatography (GC). GC analyses were performed using Shimadzu GC-2014 equipped with a barrier ionization discharge (BID) detector (Shimadzu BID-2010 Plus). Detected chemical species were identified by the retention time and quantified by the calibration curves of a set of standard samples of known concentrations.

2.5. Gas adsorption measurements. Gas adsorption isotherms of N_2 were measured using a Microtrac-BEL BELSORP mini X at 77 K. The powders of M(pz)[M'(CN)$_4$] were evacuated at 373 K for 1 hour prior to the measurement.

2.6. Field emission scanning electron microscope (FE-SEM). The microstructures of powder samples were observed by a Hitachi S-4800 FE-SEM with an accelerating voltage of 5.0 kV. The powder samples were coated with graphite by spattering prior to the SEM observation.

2.7. Acetalization reaction. Solid M(pz)[M'(CN)$_4$] (80.0 μmol) was suspended in 4 mL dry MeOH (24.7 mol L^{-1}). To the suspension was added 165 μL of cyclohexanone (1.60 mmol). The mixture was continuously stirred at 600 rpm at 296 K. The reaction was monitored by sampling 0.15 mL of the suspension at appropriate intervals. The obtained suspension was filtered and diluted by 10 times with MeOH before analyzed by gas chromatography. Acetalization catalyzed by the MCM-41 type aluminosilicate (M41-Al) was performed similarly using 30.0 mg of M41-Al. Acetalization reaction under different solvent conditions were performed similarly using the 1 : 1 and 1 : 3 mixtures of MeOH and DCM (vol/vol) instead of pure MeOH.

2.8. Filtrate test. After two hours of acetalization reaction, the reaction mixture was centrifuged at 3500 rpm for 10 minutes. The supernatant was decanted, and then filtered with a nylon syringe filter (pore size 0.22 μm) to remove solid catalysts. The filtrate was sampled at appropriate intervals and analyzed by gas chromatography.

2.9. X-ray pair distribution functions (X-ray PDFs). X-ray PDFs were collected at the beamline BL04B2 in Spring-8. The X-ray scattering data were collected on a horizontal two axis diffractometer using monochromated X-rays at 61.3 keV.

3. Results and Discussion

3.1. Metal ion dependence of defect formation. Six powder samples of 3D Hofmann-type CPs were prepared according to modified literature procedures with M = Fe^{2+}, Co^{2+}, Ni^{2+} and M' = Pd^{2+}, Pt^{2+}.[15] The phase purity of all powder samples was confirmed by powder X-ray diffraction (PXRD, Figure S1). The six compounds are isostructural, and the octahedral M ions are surrounded by CN^- and pz ligands. Having strong- and weak- field ligands in the horizontal and vertical directions, respectively, the structure is characterized by the anisotropic bonding interactions around the M ion (Figure 1B). It is therefore plausible that the anisotropy affords preferential ligand exchange on the weaker-field ligands. Indeed, a selective post-synthetic exchange of a pillar ligand was reported in a 3D Hofmann-type CP.[14]

We investigated post-synthetic exchange of the pz ligand by MeOH, another weak-field ligand, at ambient temperature. The six powders of **MM'** were immersed in excess MeOH, and then the supernatants were filtered to collect UV-Vis absorption spectra (Figure 2A). The filtrates from **MM'** powders all showed absorption around 260 and 310 nm. The absorption feature well overlaps with that of pz solution in MeOH, suggesting that the pz ligands in **MM'** come out when exposed to excess MeOH molecules (Figure S2). Importantly, the PXRD patterns of the Hofmann CPs measured after the ligand exchange were nearly identical with the pristine patterns, indicating that the periodic 3D structures are intact (Figure S3). We surmise that the vacancies formed on the pz sites were compensated by the MeOH molecules that keep the octahedral geometry of the M ions through the coordination on the O atoms (Figure 2B), resulting in the chemical formula M(pz)$_{1-x}$(MeOH)$_{2x}$[M'(CN)$_4$] ($0 < x < 0.3$). The partial ligand exchange thus affords defective coordination environment around the M ions.

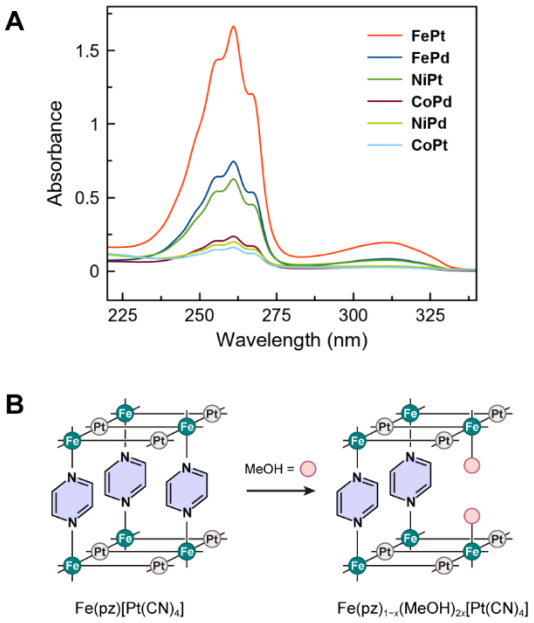

Figure 2. (A) UV-Vis absorption spectra of the filtrates obtained from **MM'**/MeOH suspensions. (B) Schematic illustration of the defect formation in **FePt** induced by MeOH. The cyanide ligands are omitted for clarity.

The amount of the pz ligands that come out of **MM'** was highly dependent on the combinations of M and M' ions. The UV-Vis absorption spectra allow us to estimate the concentration of the pz molecules, ranging from ca. 0.7 mmol L^{-1} (**CoPt**) to 6 mmol L^{-1} (**FePt**) from the 20 mmol L^{-1} suspension of **MM'** (Table 1). The concentrations differ by more than 8 times, suggesting that the species at the M site have the primary influence on the ligand exchange. Since the concentration for **FePd** (3 mmol L^{-1}) is about the half of **FePt**, the M' site is also responsible for the ligand exchange. Although the M' ions are not directly bonded to the pz ligands, they affect the electronic states of the M ions through the CN bridge, which was verified in their magnetic behaviors.[15, 18] The ligand exchange in **FePt**

corresponds to ca. 30% replacement of the pz ligands to MeOH molecules. The exchange was not complete, but the ratio is significant considering that the MeOH is a weak-field ligand. We suppose that the exchange was not complete because of a backward reaction in which the eluted pz ligands went back to the solid structure.

Table 1. Concentration of the pz molecules observed from MM' / MeOH suspensions

MM'	FePt	FePd	CoPt	CoPd	NiPt	NiPd
[pz] (mmol L^{-1})	5.9(3)	2.6(1)	0.7(2)	0.8(1)	2.3(1)	0.9(2)

3.2. Characterization of defective CPs. While the defect formation in **FePt** and **FePd** replaced more than 10% of pz ligands, the elusion of the metal ions was remarkably low. We did not observe the characteristic UV-Vis absorption features of $[Pt(CN)_4]^{2-}$ or $[Pd(CN)_4]^{2-}$ in the spectra of the **FeM'**/MeOH suspensions (Figure S2). In addition, the inductively coupled plasma-optical emission spectroscopy (ICP-OES) analyses of these filtrates found that the concentrations of the Pd and Pt ions were only 0.07 and 0.24 ppm for **FePt** and **FePd**, respectively, which are negligible compared to those of pz molecules (ca. 480 ppm for **FePt**). The large difference in the elusion concentration stems from the anisotropy in the bonding interaction in the coordination frameworks.

Field emission scanning electron microscope images (FE-SEM) of **FePt** and **FePd** powders before and after the ligand exchange revealed that there were no remarkable changes in the overall crystal sizes and morphologies (Figure S4), indicating that the ligand exchange reactions are not accompanied by dissolution and recrystallization of the metal and cyanide ions. The ligand exchange in **FePt** and **FePd** developed streaky features on the surfaces of these crystals, which run two dimensionally parallel to a crystal facet (Figure 3). We assume that the streaks were caused by the large-scale defects that formed at the pz site. The substantial ligand exchange in the *ab* plane of the crystals well explains the streaky features. FE-SEM images of the other powders revealed that **CoPd** and **CoPt** typically had crystal size about a few micrometers (a similar range to **FePd** and **FePt**), whereas **NiPd** and **NiPt** were about a few hundred nanometers (Figure S5). Notably, **FePd**, **FePt**, **CoPd**, and **CoPt** exhibited very different ligand exchange ratios despite having a similar crystal size, and **NiPd** exhibited a smaller ligand exchange ratio despite having a smaller crystal size. Although crystal size often affects defect formation at interface, we did not observe a clear correlation between the crystal size and defect density. We infer that this is because M(pz)[M'$(CN)_4$] are porous to methanol[20, 21] and the ligand exchange propagates deep into the crystals regardless of the particle size.

Adsorption isotherms of N_2 on **FePt** and **FePd** powders before and after the ligand exchange were collected to estimate the effect of defect formation on the porosity (Figure S6). The amount of adsorption was slightly decreased both for **FePt** and **FePd** after the ligand exchange, which was attributed to the loss of the micropore caused by the local disorder observed in the FE-SEM images. However, the drop was small compared to the defect concentrations, suggesting that the defect formation does not have a strong influence on the porosity of **MM'**.

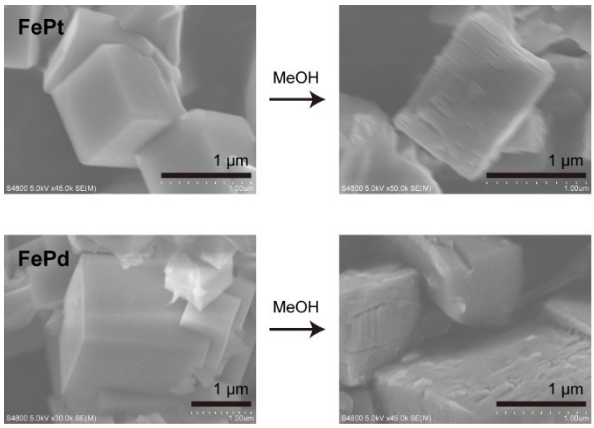

Figure 3. FE-SEM images of **FePt** and **FePd** powders before and after MeOH immersion.

3.3. Spin-coupled defect formation in FePd. Since **FeM'** are magnetic materials, we explored a spin-coupled defect formation in **FePd**. The cooperative spin crossover of **FeM** is accompanied by a discontinuous structural change, and the magnetic state depends on its thermal history and guest molecules adsorbed in the pore of **FeM**.[20, 21] The thermal hysteresis allows the material to take high-spin (HS) or low-spin (LS) states on the Fe^{2+} site at an identical temperature, depending on the thermal path (heating or cooling) the material takes to reach the temperature. In the case of **FePd** powder, HS and LS states were found to be bistable at 273 K in MeOH, suggested by the color of the powder suspensions (Figure 4A) and PXRD patterns taken as suspensions in MeOH at 273 K (Figure S7). Thus, we could compare defect formation in **FePd** at HS (**FePd**-HS) and LS (**FePd**-LS) states at the same temperature.

UV-Vis absorption spectra of the filtrate obtained from the **FePd**-LS suspension showed much smaller absorbance than that of the **FePd**-HS filtrate, indicating that the **FePd**-LS powder is less susceptible to the ligand exchange reaction (Figure 4B, see Supporting Information for the detailed procedure). The defect concentration in **FePd**-LS was estimated from the absorbance of the pz ligands to be 0.1 mmol L^{-1}, which is about 20 times smaller than that in **FePd**-HS at 273 K. The suppressed defect formation in **FePd**-LS can be understood on the basis that the t_{2g} orbitals of the Fe^{2+} ion, which are more occupied in the LS state, have more bonding character than the e_g orbitals.[22] Thus, we infer that the bonding energy between the Fe^{2+} ion and pz ligand is higher for the LS state, leading to the suppressed defect concentration in **FePd**-LS. The result suggests that we can control the defect concentration in the Hofmann CPs by manipulating the spin state. The spin-coupled defect formation is interesting in the sense that a relatively weak interaction (magnetic ordering) is transferred to a phenomenon dominated by a much stronger interaction (chemical bonds).

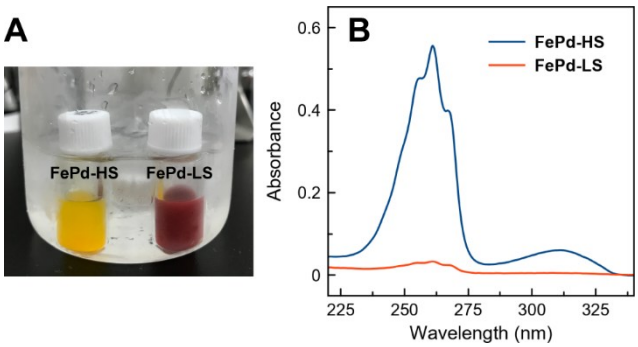

Figure 4. (A) Photograph of **FePd**-HS and **FePd**-LS suspensions in MeOH stabilized at 273 K (ice bath). (B) UV-Vis absorption spectra of the filtrates obtained from the **FePd**-HS and **FePd**-LS suspensions in MeOH.

3.4. Solvent dependence of defect formation. Since the **FePt** powder is most susceptible to the ligand exchange in MeOH, we examined the defect formation in **FePt** caused by other organic solvents. The **FePt** powder was suspended in six organic solvents (EtOH, IPA, acetone, THF, MeCN, and DCM) and the filtrates were analyzed by gas chromatography (GC) to quantify the concentrations of pz exchanged by the solvents. As shown in Figure 5, detectable amount of pz was observed in all organic solvents except for DCM. However, the concentration was much lower than that of **FePt**/MeOH suspension. IPA gave the highest concentration of pz (ca. 0.5 mmol L^{-1}) among the six organic solvents, which, however, was less than 10% of the amount from the MeOH suspension. The fact that DCM does not create vacancies at the pz site corroborate the ligand-exchange mechanism of the defect formation. The other solvents have coordination sites on the O or N atoms that can replace the pz ligands while keeping the coordination number of the M ions unchanged.

It is well known that both thermodynamic and kinetic aspects affect ligand-exchange processes in extended coordination materials.[6] While an exchange by a higher pK_a ligand would results in more stable ligand-metal coordination and is thermodynamically favorable, such a correlation between pK_a and the ligand exchange efficiency was not observed in our study. It is therefore plausible that the ligand exchange in **MM'** is dominated by kinetic aspects. One of the key kinetic factors is the diffusivity of the solvents as ligands. Because the structure requires two solvent molecules to replace one pz ligand, a bulkier solvent is supposed to be more reluctant to replace the pz ligand due to the steric hinderance. We think that this is the primary factor that makes the exchange by MeOH, the smallest molecule of the solvents tested, specifically effective.

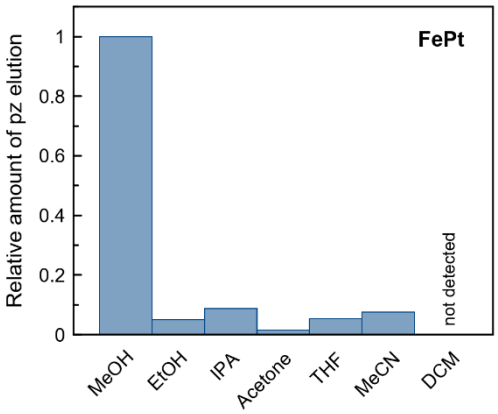

Figure 5. Relative amount of the pyrazine (pz) ligands in organic solvents eluted from **FePt**.

3.5. Acetalization catalyzed by defects. Defect engineering of CPs and MOFs accesses how to make coordinatively unsaturated sites and to tune electronic structure for catalytic applications.[23-32] To demonstrate the utility of the defect engineered CPs, we examined the catalytic activities of these powders. Since the defect concentration is specifically high in the MeOH suspension (Figure 5), we tested the acetalization of cyclohexanone in MeOH with **MM'** powders (Figure 6A). Here, MeOH serves as the solvent as well as the reactant. The reaction is slow at the ambient conditions, but readily catalyzed by Brønsted or Lewis acids.[33, 34] We chose cyclohexanone as a substrate because the size of cyclohexanone is close to that of pz. We found that three of the six CPs, **FePd**, **FePt**, and **NiPt**, showed notable activity to give 1,1-dimethoxycyclohexane and water in ca. 90% yield (24 h) without a side reaction, determined by GC (Figure 6B). On the other hand, the activity of **CoPd**, **CoPt**, and **NiPd** powders was almost negligible. We assume that the defect formation is responsible for the catalytic activity because the active group are more defective in MeOH than the inactive group (Figure 2A). The amount of the defects does not solely explain the catalytic activity, because **FePt**, which was most defective in MeOH, did not show the best catalytic performance. The quality of each active site (such as turn over frequencies) must be also considered for comprehensive explanation.

The catalysis was confirmed to be heterogenous since the reaction was shut down when the powders of the CPs were filtered out (Figure S8). The PXRD patterns of the active CPs measured after used for acetalization were nearly identical with the pristine patterns except for a broad feature observed at $2\theta \sim 20$ ° in **FePt** powder, indicating that the periodic 3D structures are intact (Figure S9). We assume that the broad feature at $2\theta \sim 20$ ° in **FePt** stems from structural disorders caused by the defect formation. Nonetheless, the X-ray pair distribution functions (PDFs) of **FePt** powders before and after the catalytic reaction were almost identical (Figure S10). We therefore conclude that the basic network connectivity of **FePt** was maintained even after the catalytic use. These filtrate tests and X-ray characterizations exclude the possibilities that the catalysis stems from small amount of the metal ions or ligands dissolved in MeOH, or unknown solid-state impurities.

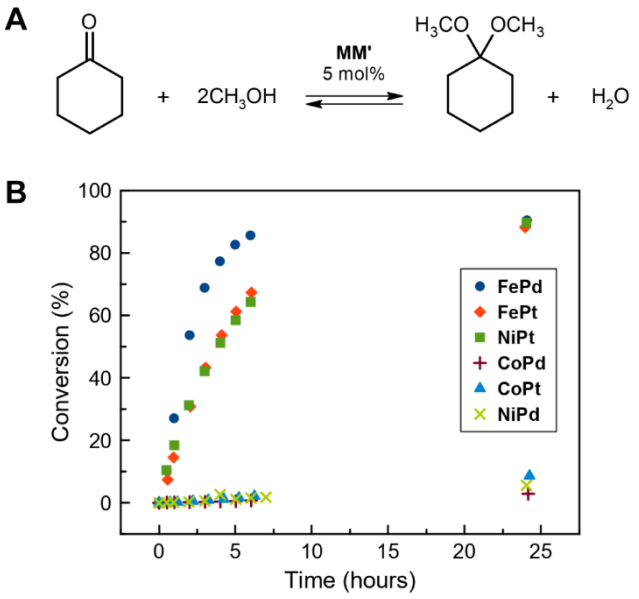

Figure 6. (A) Acetalization of cyclohexanone in the presence of the powders of **MM'**. (B) Catalytic activity of the six powders of **MM'**. Experimental conditions: cyclohexanone 1.6 mmol (0.40 mol L^{-1}), catalyst 80 μmol (0.020 mol L^{-1}), MeOH 4.0 mL, reaction temperature 296 K.

3.6. Defect engineering to control catalysis. The catalysis of **FePd**, **FePt**, and **NiPt** powders is unique in the sense that the formation of the active sites (i.e., defective sites) is induced by the reaction solvent. Because the defect concentration is highly dependent on solvent species, the catalytic activity is expected to be controlled by changing reaction solvents. We therefore examined the catalytic activity of **FePd**, the most active catalyst of the six CPs, under conditions that suppress the defect formation.

We diluted the reaction solvent (MeOH) with DCM to reduce the number of the active site, expecting the inert character of DCM as seen in the **FePt** suspension (Figure 5). Figure 7A shows the variations in the progress of acetalization catalyzed by **FePd** under different solvent conditions of MeOH : DCM = 1 : 1 and 1 : 3 in volume. We found that the reaction rate dramatically decreased upon the addition of DCM. In contrast, control reactions catalyzed by an MCM-41 type mesoporous aluminosilicate (M41-Al) showed relatively modest change in reaction rate upon the addition of DCM (Figure S11A). Note that M41-Al is a heterogenous catalyst that has implemented Lewis acidic sites (Al atoms), and that the number of the catalytic sites is not affected by the dilution. These results indicate that the deceleration of acetalization by **FePd** is attributed to the following two distinct factors; 1. the decrease in the concentration of MeOH as a reactant and 2. the decrease in the number of the catalytic sites due to the low concentration of MeOH. Indeed, GC analysis found that the concentration of the pz molecules (i.e., number of the active sites) in the **FePd** suspensions decreased by the addition of DCM (Figure S12). The result suggests that we can control the catalytic activity of **FePd** by using solvent-sensitive nature of the defect formation.

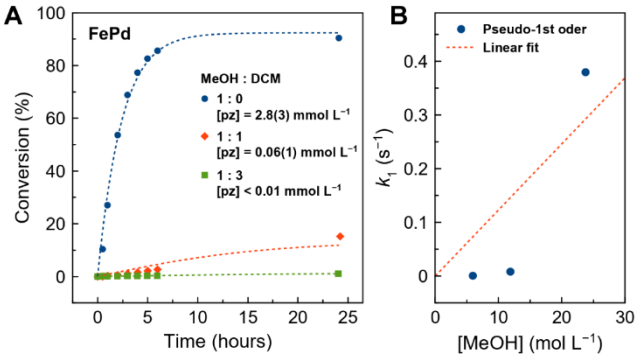

Figure 7. (A) Changes of the reaction rate of acetalization under diluted conditions catalyzed by **FePd**. The concentrations of eluted pz ligands are shown in legends on the basis of GC analysis (Figure S12). Broken lines represent simulated curves based on the kinetic model. (B) The rate constants k_1 estimated from the kinetic data of the acetalization catalyzed by **FePd**.

3.7. Kinetic analysis of defect-mediated catalysis. We used the following differential equation to estimate the rate constants of the acetalization catalyzed by the **FePd** and M41-Al powders:

$$\frac{dy}{dt} = k_1(y_0 - y) - k_2 y^2 \qquad (1)$$

where y, y_0, t, k_1, and k_2 are the concentration of 1,1-dimethylcyclohexane (the reaction product), initial concentration of cyclohexanone, time, rate constants for forward and backward reactions, respectively.[35-37] Because the MeOH molecules exist in large excess, the forward reaction is treated as a pseudo-first order reaction (see Supporting Information for more detail).

The equation (1) was numerically solved using the initial concentration of cyclohexanone, i.e., $y(0)$ = 0.4 mol L^{-1}, and thus the parameters k_1 and k_2 were optimized by non-linear least squares (broken lines in Figure 7A). The k_1 of the acetalization catalyzed by M41-Al shows a linear dependence on the concentration of MeOH (Figure S11B). The trend is consistent with the experimental condition in which the excess MeOH molecules make the forward reaction kinetics pseudo-first order. In contrast, the k_1 of the acetalization catalyzed by **FePd** considerably deviates from the linear relation with [MeOH] (Figure 7B). The deviation indicates that the concentration of MeOH affects the number of the active sites in **FePd**. These analyses are consistent with our catalytic model, corroborating the unique activation mechanism of **FePd** as a catalyst.

4. Conclusion

Systematic study on the post-synthetic ligand exchange of the 3D Hofmann-type CPs revealed that the degree of defect formation was modulated by the combination of the metal ions in the structure. Owing to the anisotropy in bonding interaction, the ligand exchange happens selectively on the weak-filed ligand, creating defective sites around the octahedral metal ions. The defect concentration reaches as high as 30% at ambient condition without dissolutions of metal ions. The defect concentration is highly dependent on the spin state of the octahedral metal ion and the solvent species for ligand exchange, giving multiple controls for defect engineering of these CPs. The defective structures function as catalysts by providing Lewis acidic sites necessary to promote the reaction. Our mechanistic

study revealed that the activity of the catalysts was controlled by the degree of defect formation, which was determined by the solvent species. Our study provides a useful insight to designing and manipulating defective structures in CPs and MOFs, and to coupling the defect engineering with properties such as magnetism and catalysis.

ASSOCIATED CONTENT

Supporting Information. PXRD patterns, UV-Vis absorption spectra, FE-SEM images, adsorption isotherms, and X-ray PDFs. This material is available free of charge via the Internet at http://pubs.acs.org.

AUTHOR INFORMATION

Corresponding Author

*E-mail: umeyama.daiki@nims.go.jp

Author Contributions

The manuscript was written through contributions of all authors.

Funding Sources

This work was supported by JSPS KAKENHI Grant Numbers JP19K21139 and JP20K15306.

Notes

The authors declare no competing financial interest.

ACKNOWLEDGMENT

PXRD and ICP-OES studies were done at the Materials Analysis Station, a shared-facility division in National Institute for Materials Science (NIMS). The synchrotron radiation experiments were performed at BL04B2 in SPring-8 with the approval of the Japan Synchrotron Radiation Research Institute (JASRI) (Proposal No. 2016B1110 and 2021A1025). We thank Dr. Satoshi Tominaka (NIMS) for discussion and measurement for X-ray total scattering experiments. We thank Dr. Yusuke Ide (NIMS) for access to equipment.

REFERENCES

1. Yaghi, O. M.; O'Keeffe, M.; Ockwig, N. W.; Chae, H. K.; Eddaoudi, M.; Kim, J. Reticular Synthesis and the Design of New Materials. *Nature* **2003**, *423*, 705-714.
2. Kitagawa, S.; Kitaura, R.; Noro, S. Functional Porous Coordination Polymers. *Angew. Chem., Int. Ed.* **2004**, *43*, 2334-2375.
3. Ferey, G. Hybrid Porous Solids: Past, Present, Future. *Chem. Soc. Rev.* **2008**, *37*, 191-214.
4. Horike, S.; Shimomura, S.; Kitagawa, S. Soft Porous Crystals. *Nature Chem.* **2009**, *1*, 695-704.
5. Fang, Z.; Bueken, B.; De Vos, D. E.; Fischer, R. A. Defect-Engineered Metal-Organic Frameworks. *Angew. Chem., Int. Ed.* **2015**, *54*, 7234-7254.
6. Deria, P.; Mondloch, J. E.; Karagiaridi, O.; Bury, W.; Hupp, J. T.; Farha, O. K. Beyond Post-Synthesis Modification: Evolution of Metal–Organic Frameworks via Building Block Replacement. *Chem. Soc. Rev.* **2014**, *43*, 5896-5912.
7. Burnett, B. J.; Barron, P. M.; Hu, C.; Choe, W. Stepwise Synthesis of Metal–Organic Frameworks: Replacement of Structural Organic Linkers. *J. Am. Chem. Soc.* **2011**, *133*, 9984-9987.
8. Karagiaridi, O.; Bury, W.; Sarjeant, A. A.; Stern, C. L.; Farha, O. K.; Hupp, J. T. Synthesis and Characterization of Isostructural Cadmium Zeolitic Imidazolate Frameworks via Solvent-Assisted Linker Exchange. *Chem. Sci.* **2012**, *3*, 3256-3260.
9. Karagiaridi, O.; Lalonde, M. B.; Bury, W.; Sarjeant, A. A.; Farha, O. K.; Hupp, J. T. Opening ZIF-8: A Catalytically Active Zeolitic Imidazolate Framework of Sodalite Topology with Unsubstituted Linkers. *J. Am. Chem. Soc.* **2012**, *134*, 18790-18796.
10. Kim, M.; Cahill, J. F.; Su, Y.; Prather, K. A.; Cohen, S. M. Postsynthetic Ligand Exchange as a Route to Functionalization of 'Inert' Metal–Organic Frameworks. *Chem. Sci.* **2012**, *3*, 126-130.
11. Kim, S.; Dawson, K. W.; Gelfand, B. S.; Taylor, J. M.; Shimizu, G. K. H. Enhancing Proton Conduction in a Metal–Organic Framework by Isomorphous Ligand Replacement. *J. Am. Chem. Soc.* **2013**, *135*, 963-966.
12. Hong, D. H.; Suh, M. P. Enhancing CO_2 Separation Ability of a Metal-Organic Framework by Post-Synthetic Ligand Exchange with Flexible Aliphatic Carboxylates. *Chem. Eur. J.* **2014**, *20*, 426-434.
13. Fan, Z.; Wang, J.; Wang, W.; Burger, S.; Wang, Z.; Wang, Y.; Wöll, C.; Cokoja, M.; Fischer, R. A. Defect Engineering of Copper Paddlewheel-Based Metal–Organic Frameworks of Type NOTT-100: Implementing Truncated Linkers and Its Effect on Catalytic Properties. *ACS Appl. Mater. Interfaces* **2020**, *12*, 37993-38002.
14. Gong, Y.; Han, W.-K.; Lu, H.-S.; Hu, Q.-T.; Tu, H.; Li, P.-N.; Yan, X.; Gu, Z.-G. Single Crystal to Single Crystal Transformation of Spin-Crossover Coordination Polymers from 3D Frameworks to 2D Layers. *J. Mater. Chem. C* **2021**, *9*, 5082-5087.
15. Niel, V.; Martinez-Agudo, J. M.; Muñoz, M. C.; Gaspar, A. B.; Real, J. A. Cooperative Spin Crossover Behavior in Cyanide-Bridged Fe(II)−M(II) Bimetallic 3D Hofmann-like Networks (M = Ni, Pd, and Pt). *Inorg. Chem.* **2001**, *40*, 3838-3839.
16. Molnár, G.; Niel, V.; Real, J.-A.; Dubrovinsky, L.; Bousseksou, A.; McGarvey, J. J. Raman Spectroscopic Study of Pressure Effects on the Spin-Crossover Coordination Polymers $Fe(Pyrazine)[M(CN)_4]\cdot 2H_2O$ (M = Ni, Pd, Pt). First Observation of a Piezo-Hysteresis Loop at Room Temperature. *J. Phys. Chem. B* **2003**, *107*, 3149-3155.
17. Tayagaki, T.; Galet, A.; Molnár, G.; Muñoz, M. C.; Zwick, A.; Tanaka, K.; Real, J.-A.; Bousseksou, A. Metal Dilution Effects on the Spin-Crossover Properties of the Three-Dimensional Coordination Polymer $Fe(pyrazine)[Pt(CN)_4]$. *J. Phys. Chem. B* **2005**, *109*, 14859-14867.
18. Ohtani, R.; Yoneda, K.; Furukawa, S.; Horike, N.; Kitagawa, S.; Gaspar, A. B.; Munoz, M. C.; Real, J. A.; Ohba, M. Precise Control and Consecutive Modulation of Spin Transition Temperature Using Chemical Migration in Porous Coordination Polymers. *J. Am. Chem. Soc.* **2011**, *133*, 8600-8605.
19. Yamada, Y.; Yoneda, M.; Fukuzumi, S. High Power Density of One-Compartment H_2O_2 Fuel Cells Using Pyrazine-Bridged $Fe[M^C(CN)_4]$ ($M^C = Pt^{2+}$ and Pd^{2+}) Complexes as the Cathode. *Inorg. Chem.* **2014**, *53*, 1272-1274.
20. Ohba, M.; Yoneda, K.; Agustí, G.; Muñoz, M. C.; Gaspar, A. B.; Real, J. A.; Yamasaki, M.; Ando, H.; Nakao, Y.; Sakaki, S.; Kitagawa, S. Bidirectional Chemo-Switching of Spin State in a Microporous Framework. *Angew. Chem., Int. Ed.* **2009**, *48*, 4767-4771.
21. Southon, P. D.; Liu, L.; Fellows, E. A.; Price, D. J.; Halder, G. J.; Chapman, K. W.; Moubaraki, B.; Murray, K. S.; Létard, J.-F.; Kepert, C. J. Dynamic Interplay between Spin-Crossover and Host−Guest Function in a Nanoporous Metal−Organic Framework Material. *J. Am. Chem. Soc.* **2009**, *131*, 10998-11009.

22. Atkins, P. W. d-Metal complexes: electronic structure and properties. In *Shriver and Atkin's Inorganic Chemistry*, 5th ed.; Oxford University Press, 2010; pp 473-506.
23. Lee, J.; Farha, O. K.; Roberts, J.; Scheidt, K. A.; Nguyen, S. T.; Hupp, J. T. Metal–Organic Framework Materials as Catalysts. *Chem. Soc. Rev.* **2009**, *38*, 1450-1459.
24. Peeters, A.; Valvekens, P.; Ameloot, R.; Sankar, G.; Kirschhock, C. E. A.; De Vos, D. E. Zn–Co Double Metal Cyanides as Heterogeneous Catalysts for Hydroamination: A Structure–Activity Relationship. *ACS Catal.* **2013**, *3*, 597-607.
25. Dissegna, S.; Epp, K.; Heinz, W. R.; Kieslich, G.; Fischer, R. A. Defective Metal-Organic Frameworks. *Adv. Mater.* **2018**, *30*, 1704501.
26. Marquez, C.; Cirujano, F. G.; Van Goethem, C.; Vankelecom, I.; De Vos, D.; De Baerdemaeker, T. Tunable Prussian Blue Analogues for the Selective Synthesis of Propargylamines through A^3 Coupling. *Catal. Sci. Technol.* **2018**, *8*, 2061-2065.
27. Bavykina, A.; Kolobov, N.; Khan, I. S.; Bau, J. A.; Ramirez, A.; Gascon, J. Metal–Organic Frameworks in Heterogeneous Catalysis: Recent Progress, New Trends, and Future Perspectives. *Chem. Rev.* **2020**, *120*, 8468-8535.
28. Chen, X.; Lyu, Y. H.; Wang, Z. Y.; Qiao, X.; Gates, B. C.; Yang, D. Tuning $Zr_{12}O_{22}$ Node Defects as Catalytic Sites in the Metal-Organic Framework hcp UiO-66. *ACS Catal.* **2020**, *10*, 2906-2914.
29. Feng, X.; Hajek, J.; Jena, H. S.; Wang, G. B.; Veerapandian, S. K. P.; Morent, R.; De Geyter, N.; Leyssens, K.; Hoffman, A. E. J.; Meynen, V.; Marquez, C.; De Vos, D. E.; Van Speybroeck, V.; Leus, K.; Van Der Voort, P. Engineering a Highly Defective Stable UiO-66 with Tunable Lewis-Bronsted Acidity: The Role of the Hemilabile Linker. *J. Am. Chem. Soc.* **2020**, *142*, 3174-3183.
30. Simonov, A.; De Baerdemaeker, T.; Bostrom, H. L. B.; Rios Gomez, M. L.; Gray, H. J.; Chernyshov, D.; Bosak, A.; Burgi, H. B.; Goodwin, A. L. Hidden diversity of vacancy networks in Prussian blue analogues. *Nature* **2020**, *578*, 256-260.
31. Wang, W.; Sharapa, D. I.; Chandresh, A.; Nefedov, A.; Heißler, S.; Heinke, L.; Studt, F.; Wang, Y.; Wöll, C. Interplay of Electronic and Steric Effects to Yield Low‐Temperature CO Oxidation at Metal Single Sites in Defect‐Engineered HKUST‐1. *Angew. Chem., Int. Ed.* **2020**, *59*, 10514-10518.
32. de Azambuja, F.; Loosen, A.; Conic, D.; van den Besselaar, M.; Harvey, J. N.; Parac-Vogt, T. N. En Route to a Heterogeneous Catalytic Direct Peptide Bond Formation by Zr-Based Metal–Organic Framework Catalysts. *ACS Catal.* **2021**, *11*, 7647-7658.
33. Tanaka, Y.; Sawamura, N.; Iwamoto, M. Highly Effective Acetalization of Aldehydes and Ketones with Methanol on Siliceous Mesoporous Material. *Tetrahedron Lett.* **1998**, *39*, 9457-9460.
34. Iwamoto, M.; Tanaka, Y.; Sawamura, N.; Namba, S. Remarkable Effect of Pore Size on the Catalytic Activity of Mesoporous Silica for the Acetalization of Cyclohexanone with Methanol. *J. Am. Chem. Soc.* **2003**, *125*, 13032-13033.
35. Chopade, S. P.; Sharma, M. M. Acetalization of Ethylene Glycol with Formaldehyde Using Cation-Exchange Resins as Catalysts: Batch versus Reactive Distillation. *React. Funct. Polym.* **1997**, *34*, 37-45.
36. Agirre, I.; Garcia, I.; Requies, J.; Barrio, V. L.; Guemez, M. B.; Cambra, J. F.; Arias, P. L. Glycerol Acetals, Kinetic Study of the Reaction Between Glycerol and Formaldehyde. *Biomass Bioenergy* **2011**, *35*, 3636-3642.
37. Singh, K.; Danieli, E.; Blumich, B. Desktop NMR Spectroscopy for Real-Time Monitoring of an Acetalization Reaction in Comparison with Gas Chromatography and NMR at 9.4 T. *Anal. Bioanal. Chem.* **2017**, *409*, 7223-7234.

Insert Table of Contents artwork here